

Topological Sensitivity Analysis for Two-Dimensional Heat Transfer Problems Using the Boundary Element Method

C. T. M. Anflor and R. J. Marczak

Abstract The objective of the current chapter is to present the application of a hard kill material removal algorithm for topology optimization of heat transfer problems. The boundary element method is used to solve the governing equations. A topological-shape sensitivity approach is used to select the points showing the lowest sensitivities, where material is removed by opening a cavity. As the iterative process evolves, the original domain has holes progressively introduced, until a given stop criteria is achieved. In a topological optimization process, final shapes with irregular boundaries are usual. Instead of applying boundary smoothing techniques at a postprocessing level, this work adopts a procedure in which smooth boundaries are ensured as a direct outcome of the original optimization code. The strategy employs Bézier curves for boundary parameterization. An algorithm is also developed to detect, during the optimization process, which curve of the intermediary topology must be smoothed. For the purpose of dealing with non-isotropic materials a linear coordinate transformation is implemented.

1 Introduction

The thermal conducting solid issue has received relatively little attention in spite of its significance for industrial applications such as polymer curing in die-molding processes, printed circuit board designs, and heat diffusers, to cite a few. Among the

C. T. M. Anflor (✉)

Campus Universitário Gama, Universidade de Brasília, Área Especial de Indústria Projeção
A-UnB-72, Brasília, DF 444–240, Brazil
e-mail: anflor@unb.br

R. J. Marczak

Departamento de Engenharia Mecânica, Universidade Federal do Rio Grande do Sul, Rua
Sarmiento Leite 425, Porto Alegre, RS 90050–170, Brazil
e-mail: rato@mecanica.ufgrs.br

numerical techniques developed for topology optimization, solid isotropic material with penalization (SIMP) and evolutionary structural optimization (ESO) rank as the dominant methods, and both (along with their variants) have been successfully used in many optimization fields (a recent comprehensive review can be found in [1]). Classical topological optimization, based on the homogenization or the density approach [2, 3], often used for elasticity problems presents some drawbacks. One of these drawbacks refers to the final and intermediary topology from an optimization process, which results an appearance of sawtooth shape boundaries. This final shape irregularity frequently requires post-processing. Final shapes obtained by sensitivity analysis using topological derivative (D_T) [4] are frequently irregular too, because of the usual methods employed to remove material. This issue independes of the optimization method adopted.

Irregularities in the boundary shape, such as those resulting from the contour of rectangular cells, are not adequate for a realistic response analysis, since a non-physical field concentration shows up around sharp corners. In order to overcome this undesired effect, and following [5], a new methodology for topology optimization is implemented in the original code. The main idea consists in smoothing the boundary during the process of optimization, that is, shape and topology optimization are simultaneously performed in the design process. A smoothing technique based on the use of Bézier curves is implemented. Afterwards the final shape is compared with those obtained through the classical optimization solution. Figure 1 illustrates a BEM mesh smoothed by Bézier interpolation.

A number of linear heat transfer examples are solved with the formulation proposed. The irregular boundaries from the final and intermediaries shapes are eliminated. Materials with non-isotropic behavior are also considered by applying the linear coordinate transformation method. The final topologies are compared to those in the literature when available.

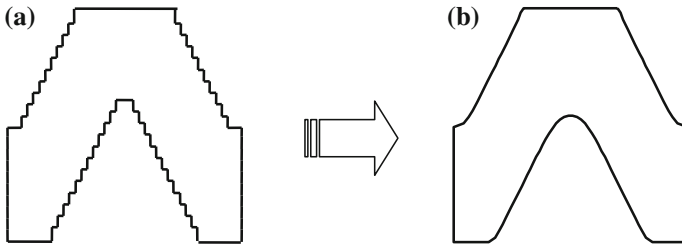


Fig. 1 Example of boundary smoothing. **a** Original result. **b** Bézier-smoothed result

2 Numerical Methodology

In this topic a schematic overview about all procedures implemented by the authors, and their sequences [6, 7] in the optimization code will be presented. The simplest BEM code is developed in its direct version using the fundamental solution for isotropic materials. The linear coordinate transformation method presented by Poon et al. [8] and Poon [9] is introduced in this routine. This technique makes it possible to solve anisotropic heat transfer problems, avoiding changes in the BEM code and manipulations of the D_T formulas. The governing differential equation for the heat conduction problem in a two-dimensional Cartesian coordinate system is given in its full form by

$$k_{11} \frac{\partial^2 T}{\partial x^2} + 2k_{12} \frac{\partial^2 T}{\partial x \partial y} + k_{22} \frac{\partial^2 T}{\partial y^2} = 0 \quad (1)$$

where, k_{11} , k_{12} , and k_{22} are the thermal conductivity coefficients, while T represents the temperature field. The corresponding heat fluxes are expressed as

$$\begin{aligned} q_x &= -k_{11} \frac{\partial T}{\partial x} - k_{12} \frac{\partial T}{\partial y} \\ q_y &= -k_{12} \frac{\partial T}{\partial x} - k_{22} \frac{\partial T}{\partial y} \end{aligned} \quad (2)$$

The initial geometry (x) established in an anisotropic medium is mapped into a corresponding geometry in an equivalent isotropic problem (\hat{x}). To do so, a special linear coordinate transformation is used, which transforms the partial differential equation into the Laplace equation, as

$$\begin{aligned} \hat{x} &= x + \alpha \cdot y \\ \hat{y} &= \beta \cdot y \end{aligned} \quad (3)$$

where $\alpha = \frac{-k_{12}}{k_{22}}$, $\beta = \frac{k}{k_{22}}$, $k = \sqrt{k_{11}k_{22} - k_{12}^2}$.

Neumann boundary conditions must also be transformed according to the Eq. (4).

$$\begin{aligned} q_y &= -k \frac{\partial T}{\partial y} = q_{\hat{y}} \\ q_x &= \beta q_{\hat{x}} - \alpha q_{\hat{y}} \end{aligned} \quad (4)$$

To demonstrate the steps of the numerical implementation, a numerical methodology scheme will be presented in details. The optimization process is carried out in 7 steps (see Fig. 2):

Step 1 Transform an orthotropic domain into an equivalent isotropic domain through the linear coordinate transformation expressed in Eq. (3). The heat flux is transformed by inverting Eq. (4).

Step 2 Solve the problems by means of the BEM code developed for isotropic materials. Evaluate D_T .

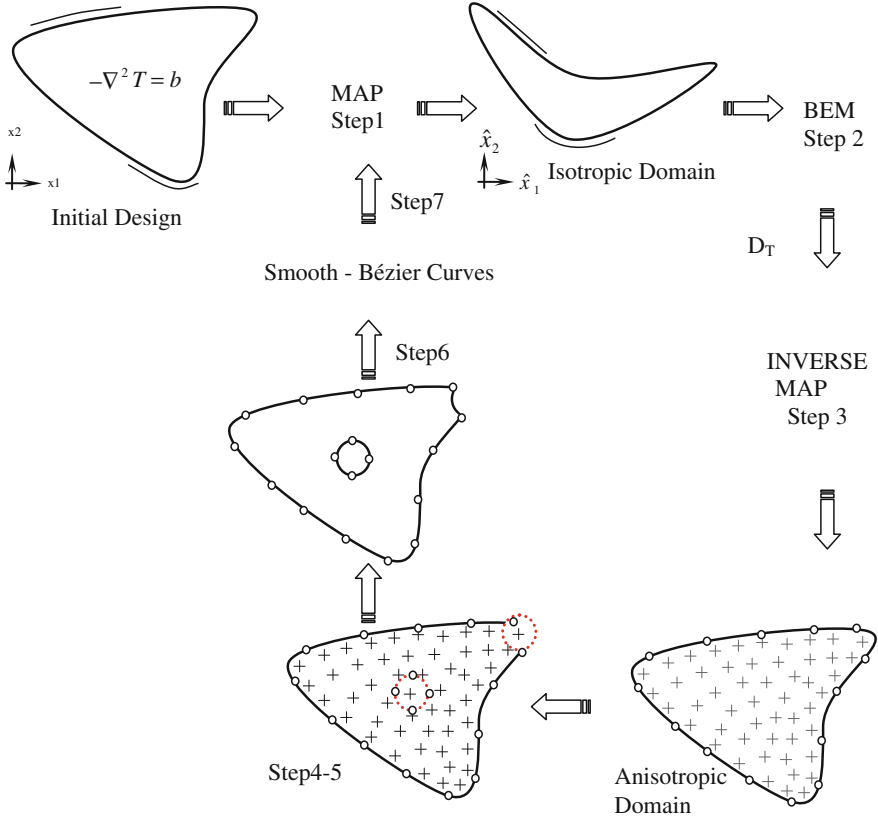


Fig. 2 Numerical methodology scheme

Step 3 Apply the inverse of the domain mapping using the equations available for the geometry and for the heat flux.

Step 4 The variables are evaluated on a suitable grid of interior points. The points with the lowest values of D_T are selected.

Step 5 Holes are created by “punching out” disks of material centered on the points previously selected.

Step 6 Smooth process using Bézier curves is introduced.

Step 7 Check stopping criteria, rebuild the mesh, return to step 1.

When the process is halted, a smooth final design topology of a non-isotropic material is expected. Note that in order to avoid geometrical boundary irregularities due to the algorithm used to remove material, a smoothing process is implemented at step 6. The smoothing technique uses Bézier curves to treat the polylines of intermediary geometries [10].

2.1 The Boundary Element Method

The formulation and application of the BEM for two-dimensional potential problems is very well established. In what follows only a brief description of the method is given. Further details can be found in [11] and [12]. Equation (5) presents the boundary integral equation which relates the potential u and flux q on the boundary Γ , in absence of body sources,

$$\frac{1}{2}u^i(x) + \int_{\Gamma} u(x)q^*(x, x')d\Gamma = \int_{\Gamma} q(x)u^*(x, x')d\Gamma \quad (5)$$

The functions u^* and q^* are the so-called potential and flux fundamental solutions due to a unit source applied at x' .

$$u^* = \frac{1}{2\pi} \int_{\Gamma} \ln\left(\frac{1}{r}\right) d\Gamma$$

$$r = \|x - x'\| \quad (6)$$

The next step consists in discretizing the problem boundary Γ using N linear boundary elements, see Fig. 3.

The values of u and q at any point on an element can be written in terms of the nodal values and the two interpolation functions ϕ_1 and ϕ_2 :

$$\begin{aligned} u(\xi) &= \phi_1 u_1 + \phi_2 u_2 = [\phi_1 \phi_2] \begin{Bmatrix} u_1 \\ u_2 \end{Bmatrix} \\ q(\xi) &= \phi_1 q_1 + \phi_2 q_2 = [\phi_1 \phi_2] \begin{Bmatrix} q_1 \\ q_2 \end{Bmatrix} \end{aligned} \quad (7)$$

where ξ is a local intrinsic coordinate defined in the range $[-1, +1]$ and ϕ_1 and ϕ_2 are the standard discontinuous linear shape functions [11]. Considering the discretized version of Eq. (5), the integral in the left hand side over the element j can be written as,

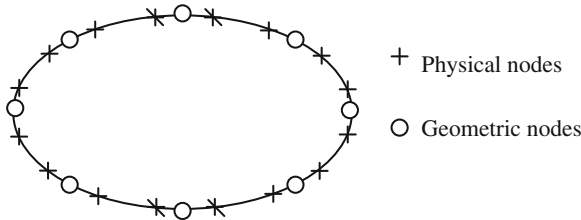


Fig. 3 Boundary element discretization

$$\int_{\Gamma_j} u q^* d\Gamma = \int_{\Gamma_j} [\phi_1 \phi_2] q^* d\Gamma \begin{Bmatrix} q_1 \\ q_2 \end{Bmatrix} = [h_1^{ij} h_2^{ij}] \begin{Bmatrix} q_1 \\ q_2 \end{Bmatrix} \quad (8)$$

where for each element j we have the two terms,

$$\begin{aligned} h_1^{ij} &= \int_{\Gamma_j} \phi_1 q^* d\Gamma \\ h_2^{ij} &= \int_{\Gamma_j} \phi_2 q^* d\Gamma \end{aligned} \quad (9)$$

Similarly, the integral on the right hand side results in

$$\int_{\Gamma_j} q u^* d\Gamma = \int_{\Gamma_j} [\phi_1 \phi_2] u^* d\Gamma \begin{Bmatrix} q_1 \\ q_2 \end{Bmatrix} = [g_1^{ij} g_2^{ij}] \begin{Bmatrix} q_1 \\ q_2 \end{Bmatrix} \quad (10)$$

where,

$$g_1^{ij} = \int_{\Gamma_j} \phi_1 u^* d\Gamma \text{ and } g_2^{ij} = \int_{\Gamma_j} \phi_2 u^* d\Gamma \quad (11)$$

After the substitution of Eqs. 11 and 9 for all the j elements in the discretized counterpart of Eq. 5, results:

$$c^i u^i + \sum_{j=1}^N H^{ij} u^j = \sum_{j=1}^{2N} G^{ij} q^j \quad (12)$$

After the imposition of all boundary conditions, the system in Eq. (12) can be reordered in such a way that all the unknowns are taken to the left hand side, resulting in the following system of equations:

$$[A]\{X\} = \{F\} \quad (13)$$

2.2 Topological Derivative

Topological derivative for Laplace and Poisson equations are applied in this work. A simple example of applicability consists in a case where a small hole of radius (ε) is open inside the domain. The concept of D_T consists in determining the sensitivity of a given cost function (ψ) when this small hole is increased or decreased (Fig. 4).

The local value of D_T at a point (\hat{x}) inside the domain for this case is evaluated by:

$$D_T^*(\hat{x}) = \lim_{\varepsilon \rightarrow 0} \frac{\psi(\Omega_\varepsilon) - \psi(\Omega)}{f(\varepsilon)} \quad (14)$$

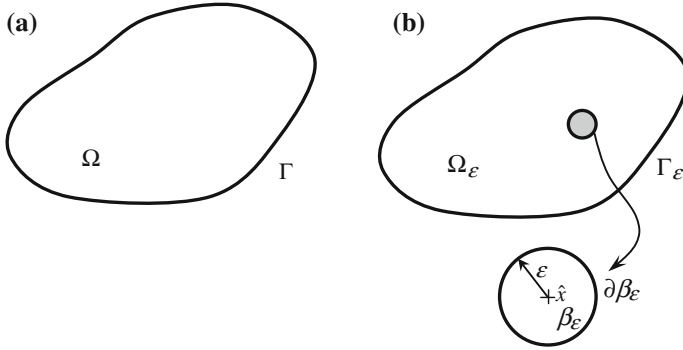


Fig. 4 Topological derivative original concept: **a** original domain Ω and **b** perturbed domain Ω_ε

where $\psi(\Omega)$ and $\psi(\varepsilon)$ are the cost function evaluated for the original and the perturbed domain, respectively, and is a problem dependent regularizing function. By Eq. (14) it is not possible to establish an isomorphism between domains with different topologies. This equation was modified introducing a mathematical idea that the creation of a hole can be accomplished by perturbing an existing one whose radius tends to zero, Fig. 5.

This allows the restatement of the problem in such a way that it is possible to establish a mapping and obtain an expression for the topological derivative, such that

$$D_T^*(\hat{x}) = \lim_{\varepsilon \rightarrow 0} \frac{\psi(\Omega_{\varepsilon+\delta\varepsilon}) - \psi(\Omega_\varepsilon)}{f(\Omega_{\varepsilon+\delta\varepsilon}) - f(\Omega_\varepsilon)} \quad (15)$$

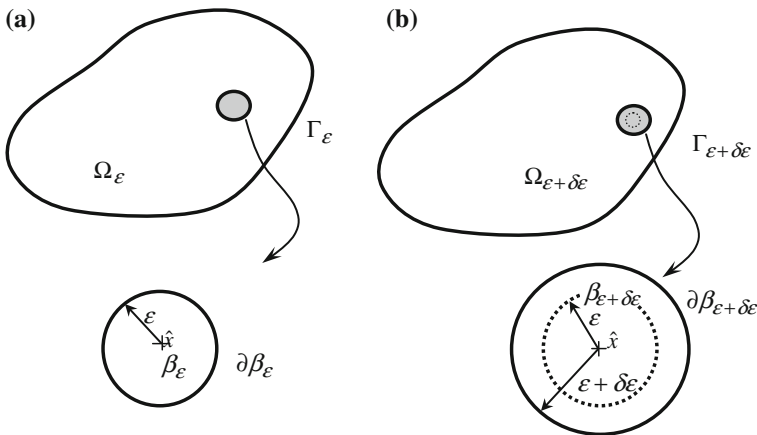


Fig. 5 Topological derivative with a new point of view. **a** Original domain and **b** perturbed domain

where δ_ε is a small perturbation on the holes's radius. Equation (15) gives a shape sensitivity when the hole becomes larger or smaller. It is also important to notice the both Eqs. 14, 15 are equivalent, as presented in [4]. The D_T for the steady state heat transfer will be briefly reviewed herein. In the case of linear heat transfer, the direct problem is stated as:

$$\text{Solve } \{u_\varepsilon | -k \Delta u_\varepsilon = b\} \text{ on } \Omega_\varepsilon \quad (16)$$

subjected to

$$\begin{cases} u_\varepsilon = \bar{u} & \text{on } \Gamma_D \\ k \frac{\partial u}{\partial n} = \bar{q} & \text{on } \Gamma_N \\ k \frac{\partial u_\varepsilon}{\partial n} = h_c (u_\varepsilon - u_\infty) & \text{on } \Gamma_R \end{cases} \quad (17)$$

where

$$h(\alpha, \beta, \gamma) = \underbrace{\alpha (u_\varepsilon - \bar{u}^\varepsilon)}_{\text{Dirichlet b.c.}} + \underbrace{\beta \left(k \frac{\partial u_\varepsilon}{\partial n} + \bar{q}^\varepsilon \right)}_{\text{Neumann b.c.}} + \underbrace{\gamma \left(k \frac{\partial u_\varepsilon}{\partial n} + h_c^\varepsilon (u_\varepsilon - u_\infty^\varepsilon) \right)}_{\text{Robin b.c.}} = 0 \quad (18)$$

is a function which takes into account the type of boundary condition on the holes to be created ($u_\varepsilon, \frac{\partial u_\varepsilon}{\partial n} = q_\varepsilon$ are the temperature and flux on the hole boundary, while u_∞^ε and h_c^ε are the hole's internal convection parameters, respectively).

A general form for the cost function can be written as

$$\psi(\Omega_\tau) = \int_{\Omega_\tau} \varphi_{\Omega_\tau}(u_\tau) d\Omega_\tau + \int_{\Gamma_\tau} \varphi_{\Gamma_\tau}(u_\tau) d\Gamma_\tau \quad (19)$$

where τ is a parameter associated to the shape change velocity, i.e., $x_\tau(x) = x + \tau v(x)$. The sensitivity of the cost function with respect to τ can be derived from the Gâteaux derivative.

$$\frac{d}{d\tau} \Psi(\Omega_\tau)_{\tau=0} = \lim_{\tau \rightarrow 0} \frac{\Psi(\Omega_\tau) - \Psi(\Omega_{\tau| \tau=0})}{\tau} h(\alpha, \beta, \gamma) = 0 \text{ on } \partial\beta_\varepsilon \quad (20)$$

Therefore the problem should be re-stated as

Evaluate: $\frac{d}{d\tau} \Psi(\Omega_\tau) = 0$

Subject to

$$a_\tau(u_\tau, n_\tau) = l_\tau(n_\tau) \quad \forall n_\tau \in \beta_{\tau 1} \quad \forall \tau \geq 0 \quad (21)$$

where a_τ is a continuous, coercive bilinear form, l_τ is a continuous linear functional and β_τ is the space of the admissible perturbation functions for the perturbed domain Ω_τ . Using the total potential energy as a cost function ($\Phi_\tau(u_\tau) := \frac{1}{2} a_\tau(u_\tau, u_\tau) - l(u_\tau)$), the bilinear form a_τ and the functional l_τ are written as:

$$\begin{aligned}
a_\varepsilon(u_\varepsilon, n_\varepsilon) &:= \int_{\Omega_\varepsilon} k \nabla u_\varepsilon \cdot \nabla \eta_\varepsilon d\Omega + \int_{\Gamma_c} h_c u_\varepsilon \eta_\varepsilon d\Gamma + \int_{\partial \Lambda_\varepsilon} h_c^\varepsilon u_\varepsilon \eta_\varepsilon d\partial \Lambda \\
l_\varepsilon(\eta_\varepsilon) &:= \int_{\Omega_\varepsilon} b \eta_\varepsilon d\Omega - \int_{\Gamma} \bar{q} \eta_\varepsilon d\Gamma - \int_{\Gamma_c} h_c u_\infty \eta_\varepsilon d\Gamma - \int_{\partial \Lambda_\varepsilon \bar{q}_\varepsilon} \eta_\varepsilon d\partial \Lambda + \gamma \int_{\partial \Lambda_\varepsilon} h_c^\varepsilon u_\infty \eta_\varepsilon d\partial \Lambda
\end{aligned} \quad (22)$$

Considering Eq. (21) one can derive the D_T expression particularized for the three classical boundary conditions prescribed on the holes.

2.2.1 Neumann Boundary Condition

For this case, Eq. (9) is particularized as $(\alpha = 0, \beta = 1, \gamma = 0)$ and the D_T is obtained by taking the limit:

$$D_T(\hat{x}) = - \lim_{\varepsilon \rightarrow 0} \frac{1}{2f'(\varepsilon)} \int_{\partial \Omega_\varepsilon} \left[k \left(\frac{\partial u_\varepsilon}{\partial t} \right) - k \left(\frac{\partial u_\varepsilon}{\partial n} \right) - 2bu_\varepsilon - \frac{2}{\varepsilon} \bar{q}_\varepsilon u_\varepsilon \right] d\Omega_\varepsilon \quad (23)$$

Both cases of Neumann boundary conditions must be considered:

$$\bar{q}_\varepsilon = \frac{\partial u_\varepsilon}{\partial n} \Big|_{\partial \Omega_\varepsilon} = 0 \quad \text{with } f'(\varepsilon) = -\pi \varepsilon^2 \quad (24)$$

$$\bar{q}_\varepsilon = \frac{\partial u_\varepsilon}{\partial n} \Big|_{\partial \Omega_\varepsilon} \neq 0 \quad \text{with } f'(\varepsilon) = -2\pi \varepsilon \quad (25)$$

For homogeneous and non-homogeneous cases respectively.

2.2.2 Dirichlet Boundary Condition

For this case, Eq. (9) is particularized as $(\alpha = 1, \beta = 0, \gamma = 0)$ and the D_T is obtained by taking the limit:

$$D_T(\hat{x}) = - \lim_{\varepsilon \rightarrow 0} \frac{1}{2f'(\varepsilon)} \int_{\partial \Omega_\varepsilon} \left[k \left(\frac{\partial u_\varepsilon}{\partial t} \right)^2 - k \left(\frac{\partial u_\varepsilon}{\partial n} \right)^2 - 2bu_\varepsilon \right] d\Omega_\varepsilon \quad (26)$$

being the conditions

$$u_\varepsilon = \bar{u}_\varepsilon \quad \frac{\partial u_\varepsilon}{\partial t} \Big|_{\partial \Omega_\varepsilon} \neq 0 \quad (27)$$

used along with $f'(\varepsilon) = \frac{-2\pi}{\ln \varepsilon}$.

Table 1 Topological derivative for the three b.c. prescribed on the holes

Boundary condition on the hole	Topological derivative	Evaluated at
Neumann homogeneous boundary condition ($\alpha = 0, \beta = 1, \gamma = 0$)	$D_T(\hat{x}) = k \nabla u \nabla u - bu$	$\hat{x} \in \Omega \cup \Gamma$
Neumann non-homogeneous boundary condition ($\alpha = 0, \beta = 1, \gamma = 0$)	$D_T(\hat{x}) = -q_\varepsilon u$	$\hat{x} \in \Omega \cup \Gamma$
Robin boundary condition ($\alpha = 0, \beta = 0, \gamma = 1$)	$D_T(\hat{x}) = h_c^\varepsilon (u_\varepsilon - u_{\varepsilon\infty})$	$\hat{x} \in \Omega \cup \Gamma$
Dirichlet boundary condition ($\alpha = 1, \beta = 0, \gamma = 0$)	$D_T(\hat{x}) = -\frac{1}{2}k(u - \bar{u}_\varepsilon)$	$\hat{x} \in \Omega$
Dirichlet boundary condition ($\alpha = 1, \beta = 0, \gamma = 0$)	$D_T(\hat{x}) = k \nabla u \nabla u - b\bar{u}_\varepsilon$	$\hat{x} \in \Gamma$

2.2.3 Robin Boundary Condition

In this case one has ($\alpha = 0, \beta = 0, \gamma = 1$) and the D_T is obtained by taking the limit:

$$D_T(\hat{x}) = -\lim_{\varepsilon \rightarrow 0} \frac{1}{2f'(\varepsilon)} \int_{\partial\Omega_\varepsilon} \left[k \left(\frac{\partial u_\varepsilon}{\partial t} \right)^2 - k \left(\frac{\partial u_\varepsilon}{\partial n} \right)^2 - 2bu_\varepsilon - \frac{2}{\varepsilon} h_c^\varepsilon (u_\varepsilon - 2u_{\varepsilon\infty}) \right] d\Omega_\varepsilon \quad (28)$$

Now the regularizing function is $f'(\varepsilon) = -2\pi\varepsilon$.

Table 1 summarizes the final expressions for D_T after application of the respective regularizing functions for each boundary condition, in accordance to Eqs. (23), (26) and (28).

It is also important to take attention that D_T is evaluated by different expressions for internal and boundary points. Another remark relies on the fact that the expressions presented in Table 1 are deduced taking the total potential energy as cost function. Once the internal points have been calculated by BEM (at step 2 in Fig. 2) one can determine the domain's sensitivity by using the equations presented in Table 1. It is important to note that the D_T is calculated in the transformed domain (\hat{x}, \hat{y}) where its behavior is isotropic and the material is removed in the original domain (x, y) between steps 4-5, as depicted in Fig. 2.

2.3 Bézier Curves

Generally in an optimizations process the final topology results in a non-smooth geometry and requires the use of smoothing techniques during the optimization process. The most popular techniques to deal with these irregular geometries employ Bézier curves (adopted in this work), Douglas-Peucker and B-Splines algorithms. The Bézier curve approach was pioneered by Renault for modeling of surfaces in

automobile design [10]. Bézier defines the curve $P(u)$ in the terms of the location of $n + 1$ control points p_i .

$$P(u) = \sum_{i=0}^n p_i B_{i,n}(u) \quad (29)$$

where $B_{i,n}(u)$ are blending functions or polynomials of Bernstein

$$B_{i,n}(u) = C(n, i) u^i (1 - u)^{n-i} \quad (30)$$

and $C(n, i) = \frac{n!}{i!(n-i)!}$ are the binomial coefficients.

Here, Eq. 29 is a vector and could be expressed by writing equations for the x and y parametric functions separately:

$$\begin{aligned} x(u) &= \sum_{i=0}^n x_i B_{i,n}(u) \\ y(u) &= \sum_{i=0}^n y_i B_{i,n}(u) \end{aligned} \quad (31)$$

x_i and y_i are the coordinates of the control points of the curve, always $n + 1$ points. The union of these points form the vertices of the control polygon of the Bézier curve. These points are responsible to control the shape of the curve, with the parameter u varying between 0 to 1. Further details can be found in [13]. As exposed until here the techniques for smoothing curves are well established in the literature and there is no difficulty associated to their application. However, in an optimization problem the effort relies on identifying which portions of the intermediary topologies must be smoothed. There are some parts of the topology that cannot be smoothed, such as the portion with prescribed boundary conditions or the portion which is a straight line. In order to overcoming this problem a routine is developed in the present work to identify, during an iterative optimization process, which curves must be or not smoothened. This routine was introduced inside the optimization algorithm as step 6, after the step of material removal (see Fig. 2). Figure 6 depicts the scheme of identification and smoothing of curves that takes place during the optimization process. This is a subroutine implemented between step 5 and 7 of the original code, as illustrated in Fig. 2.

3 Numerical Results

This section presents some examples that demonstrate the application of the proposed method. The results obtained for the first example are compared to those obtained by Park [14] for isotropic materials. The second example differs from the first one only in the boundary conditions, which prescribe convection in the cavities. The third and fourth examples consist in a square domain under high and low temperature boundary

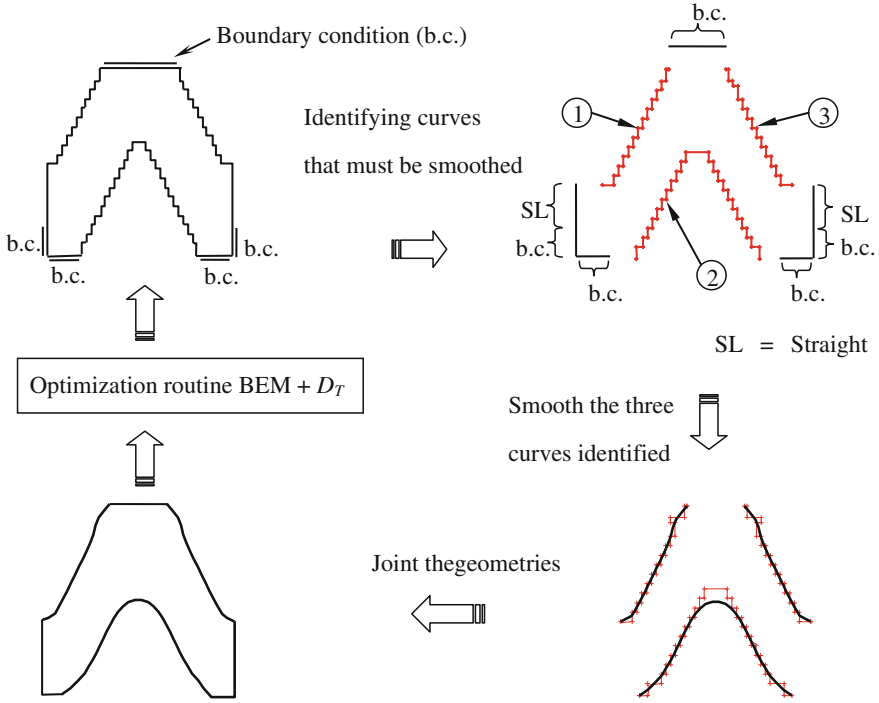


Fig. 6 Scheme of identification and smoothness—Step 6

conditions where the constitutive properties are varied to result in all possible material behaviors: isotropic, orthotropic and anisotropic. Finally, the last example considers an isotropic domain with heat sources. For this case the mapping technique and the smoothing process were not employed. The history of material removal is analyzed and illustrated for each case. The iterative process is halted when a given amount of material is removed from the original domain, regardless of the type of material medium. This criterion provides a basis to compare the topologies generated for isotropic, orthotropic and anisotropic media under the same initial geometry and boundary conditions. In all cases the total potential energy is used as the cost function. A regularly-spaced grid of internal points is generated automatically, taking into account the radius of the holes created during each iteration. The radius is obtained as a fraction of a reference dimension of the domain ($r = \omega l_{ref}$). In all cases $l_{ref} = \min(\text{height}, \text{width})$ is adopted. The objective in all cases is to minimize the material area. The current area of the domain (A_f) is checked at the end of each iteration until a reference value is achieved ($A_f = \varphi A_0$, where A_0 represents the initial area and φ a defined percentage of material to be removed). After that, the intermediary topology is smoothed by using Bézier functions. Linear discontinuous boundary elements integrated with 6 Gauss points are used in all cases.

3.1 Heat Conductor with Neumann Boundary Conditions on the Cavities

A rectangular 20×30 units domain subjected to prescribed temperature ($T_1 = 393 \text{ K}$) on its left edge and convection boundary conditions ($T_0 = 298 \text{ K}$ and $h_0 = 5.677 \text{ W/m}^2 \text{ K}$) on the remaining ones is to be optimized (Fig. 7). Here, the problem is revisited using only isotropic material properties. The isotropic material used is Aluminum ($k = 236 \text{ W/mK}$). For this case, Neumann boundary conditions are prescribed on the cavities open during the optimization process.

Figure 8 shows the evolution history obtained until the final area reached 30 % of the original value. The final and intermediary topology result in a smooth appearance shape. It is important to note that the appearance of saw-tooth shape on boundaries is avoided, discarding a post-processing in a manufacturing process.

The mean flux on the left edge side of the plate is chosen to take into account the behavior as the process evolves. The values of the mean flux obtained during the process of optimization including Bézier smoothing are recorded and compared to the result obtained with the original code with no smoothing. These results are depicted in Fig. 9 where is possible to see the evolutive iteration \times mean flux. Also, in the same figure, the smoothed intermediary topology is depicted for some iterations.

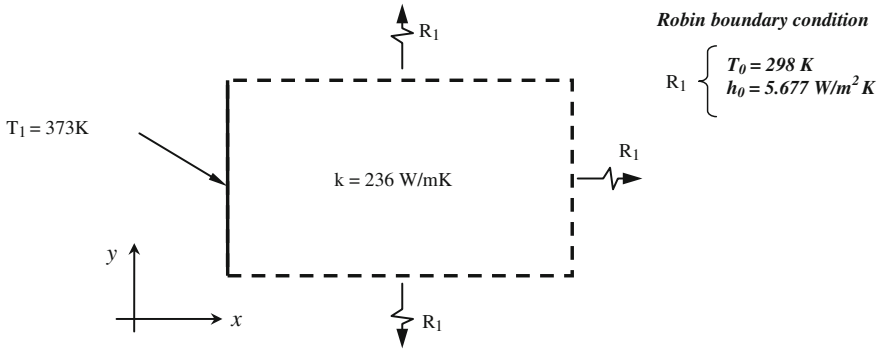


Fig. 7 Initial design domain

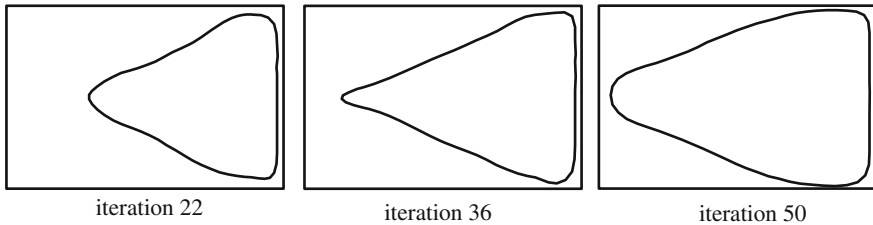


Fig. 8 Evolution history for isotropic media

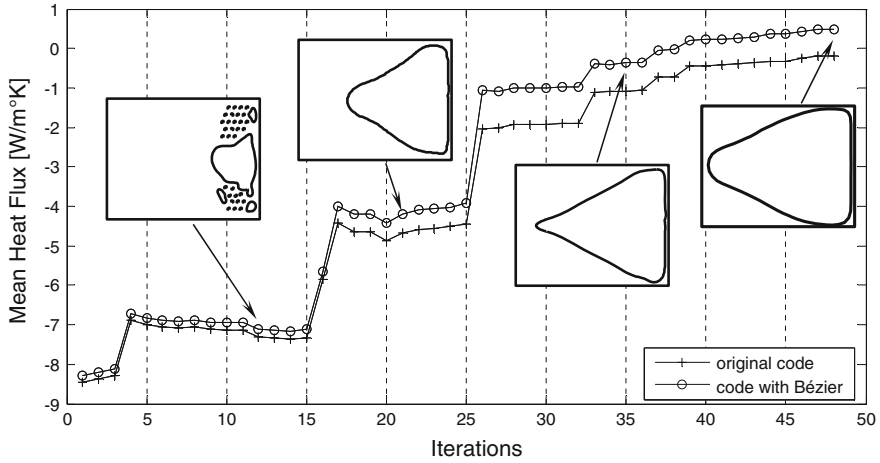


Fig. 9 Optimization history of mean heat flux versus iteration

In the orthotropic case, the thermal conductivities are imposed as $k_y/k_x = 2$. Figure 10 presents the evolution history obtained until the same volume ratio of the isotropic case was reached. Clearly, the resulting geometry of the internal cavity has a more pronounced curvature, so as to ease the heat flux in the y direction.

Park [14] solved this problem by using homogenization techniques and the FEM. Figure 11 compares the results obtained by Park [14] with the ones obtained with

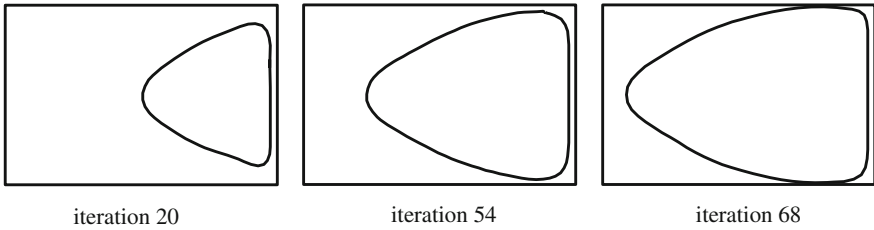


Fig. 10 Evolution history for orthotropic media

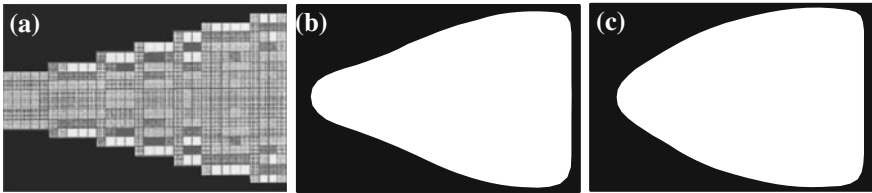


Fig. 11 Final topologies: **a** FEM+homogenization [14] – $k_x/k_y = 1$; **b** Present work, BEM+ $D_T - k_x/k_y = 1$; **c** Present work, BEM+ $D_T - k_y/k_x = 2$

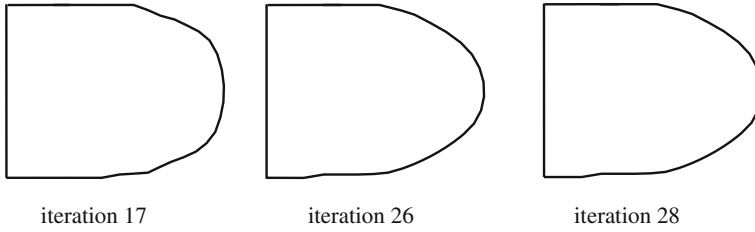


Fig. 12 Evolution history under Robin boundary conditions

the present method. In all cases, the final geometry is satisfactorily leading to a high-conductivity layout, and both isotropic results match.

3.2 Heat Conductor with Robin Boundary Conditions on the Cavities

This case is very similar to the previous one, except for the fact that the convection boundary condition is imposed on the cavities. This is an isotropic case optimized to a volume constraint of 65 % of the original design domain. The evolution of the optimization process is depicted in Fig. 12. It is important to point out that the final geometry converged to the shape of an optimal fin.

3.3 Inverted V Heat Conductor

This example consists in a square domain with high temperature (373 K) applied to its lower corners, while a low temperature (273 K) is applied at the mid top edge. The remaining boundaries are insulated. The cavities are created with $r = 0.04 l_{ref}$ and the process is halted when $A_f = 0.6A_0$ is attained. For the purpose of illustrating and comparing the final topologies obtained, three variations of the present example are studied as:

Case A :	$k_{xx} = 1;$	$k_{yy} = 1$
Case B :	$k_{xx} = 2;$	$k_{yy} = 1$
Case C :	$k_{xx} = 3;$	$k_{yy} = 1$

Figure 13 shows the results for the isotropic case (case A) which is used to compare the final design with those of the orthotropic cases (cases B and C). Figures 14 and 15

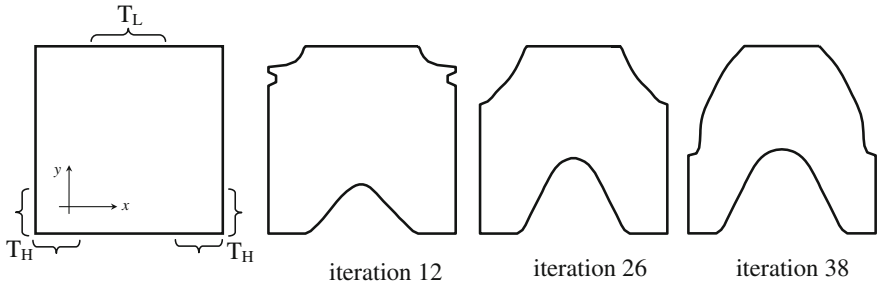


Fig. 13 Evolution history for isotropic material—Case A

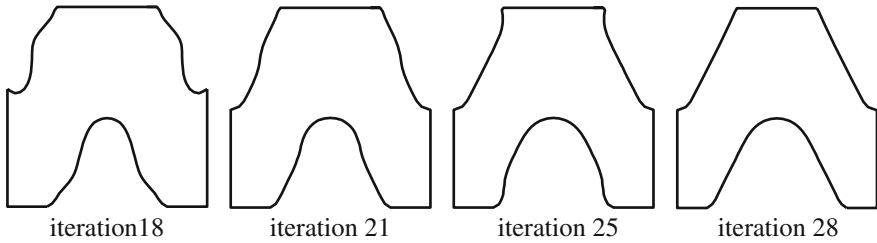


Fig. 14 Evolution history for orthotropic material—Case B

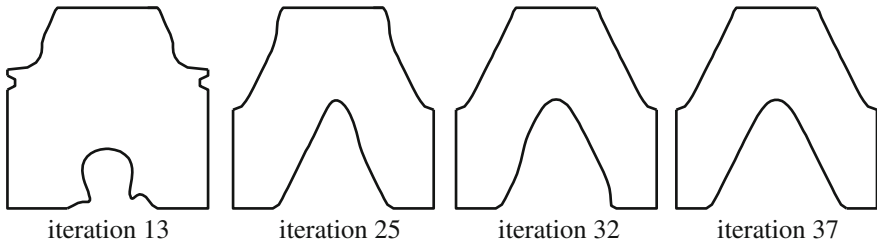


Fig. 15 Evolution history for orthotropic material—Case C

present the optimization evolution for the orthotropic cases and their final topologies when the stop criteria is achieved. From this it is possible to compare the three cases. There are visible differences in the evolution of material removal for each case. Therefore, the final designs are slightly different.

Figure 16 presents the evolution of material removal for all cases. It is found that highly orthotropic cases result in higher values of the topological sensitivity, in comparison to the isotropic solution. Consequently, a larger material removal rate is expected for orthotropic problems, in general, but this is an assertion that highly depends on the nature of the problem.

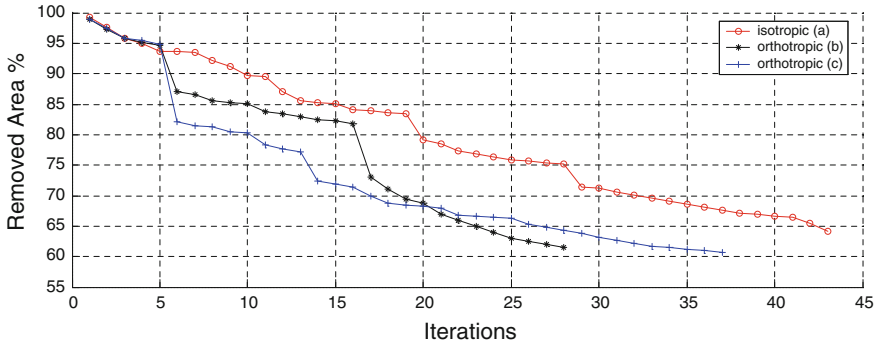


Fig. 16 Material removal history for the inverted V heat conductor

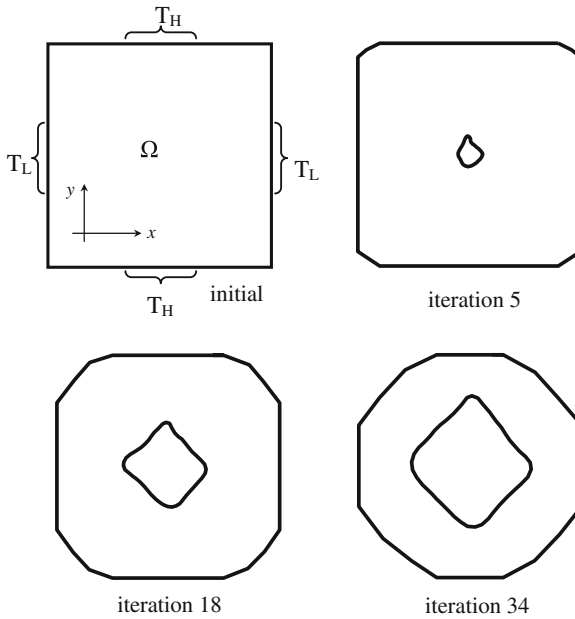


Fig. 17 Evolution history for isotropic case ($k_{11} = k_{22} = 1$)

3.4 Cross Heat Conductor

This example refers to a square domain subjected to low and high temperature boundary conditions on the middle of opposite sides. The problem is depicted in Fig. 17, where T_H is the high temperature (373 K) and T_L is the low temperature (273 K). The remaining boundaries are insulated. All possible cases are studied: isotropic, orthotropic and anisotropic materials and they are to be optimized until $A_f \approx 0.4A_0$ is achieved.

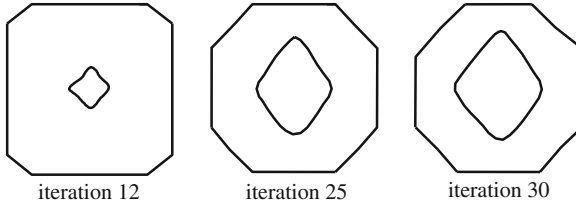


Fig. 18 Evolution history for orthotropic case ($k_{xx}/k_{yy} = 5$)

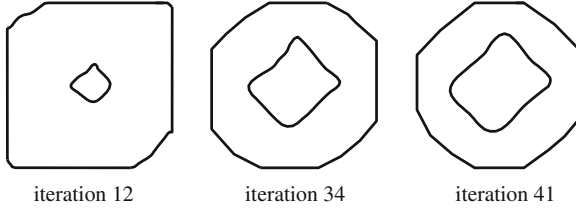


Fig. 19 Evolution history for anisotropic case ($k_{xx} = 1, k_{yy} = 1; k_{xy} = 0.5$)

Initially, an isotropic case is analyzed with $k_{11} = k_{22} = 1$. Symmetry is not used to provide a direct comparison to the subsequent anisotropic cases (which cannot use symmetry). Figure 14 also shows the evolution of material removal for $r = 0.02l_{ref}$. It is important to observe that the algorithm delivers fairly symmetric solutions throughout the process. The condition $A_f \approx 0.4 \cdot A_0$ is achieved after 34 iterations. The second case represents a highly orthotropic material, with the conductivities set to $k_{xx} = 5$ and $k_{yy} = 1$ (see Fig. 18). As expected, material is selectively removed so that the heat flux along the x direction is increased. The stop criterion $A_f \approx 0.4A_0$ is achieved after 30 iterations.

The third case considers an anisotropic material with $k_{xx} = 1, k_{yy} = 1$ and $k_{xy} = 0.5$. The evolution history is presented in Fig. 19, showing that the initial symmetry is lost after the first iterations, as expected. Contrary to the previous cases, the internal cavity results in a rhombic shape since the Cartesian axes are not parallel to the main axes of the constitutive matrix.

Figure 20 shows the percentage of material removed as a function of the number iterations for each case studied in the cross heat conductor. All cases are stopped when about 40% of material is removed. These cases are analyzed without the aid of symmetry, for comparison purposes. Obviously, anisotropic cases cannot use symmetry in general, but in many practical situations it is possible (or even expected) to align the axes of the component with the principal directions of the constitutive matrix. In such cases, smoother designs can be obtained. In order to provide a further benchmark, the cross heat conductor example is re-analyzed for the isotropic and orthotropic cases using only one quadrant of the original geometry.

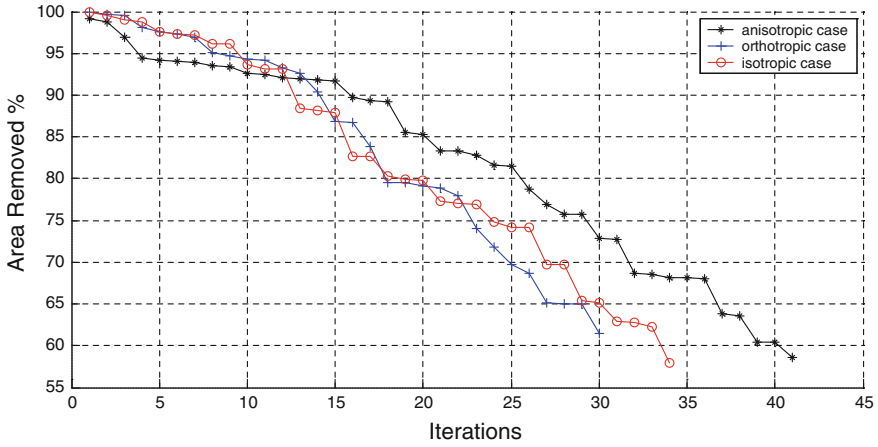


Fig. 20 Material removal history for the cross heat conductor

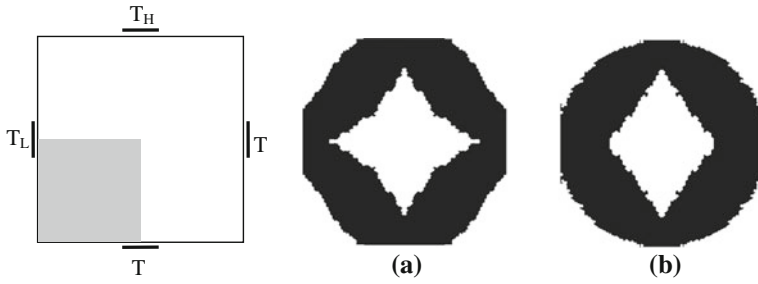


Fig. 21 Final topologies for: **a** isotropic and **b** orthotropic examples

Fig. 22 Bézier final topologies for: **a** isotropic and **b** orthotropic examples

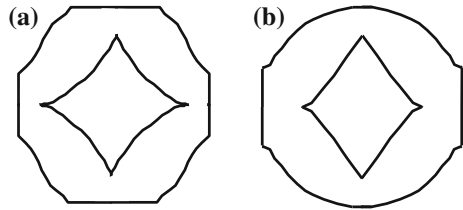


Figure 21 shows the final topologies obtained for both cases while Fig. 22 depicts the same topology after the smoothing process. The material is removed initially with $r = 0.04 l_{ref}$ and then $r = 0.02 l_{ref}$ for the remaining iterations. This simple expenditure helps generating smoother boundaries in the final design.

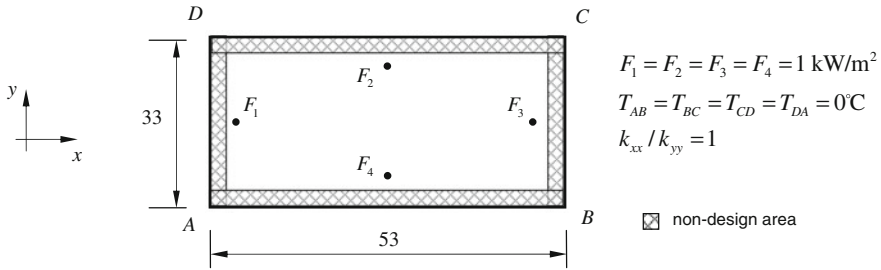


Fig. 23 PCB: initial design

3.5 Printed Circuit Board

This example was proposed by Li et al. [15] and refers to a printed circuit board (PCB) substrate. An important aspect of good PCB designs is the ability to dissipate the maximum amount of thermal energy with the minimum possible volume of material. Topology optimization is a valuable tool in such cases, allowing material savings unfeasible using only intuitive design ideas. Figure 23 shows the initial layout for this case, where four heat sources are used to simulate the heat generated by major electronic components mounted on the PCB. Part of the domain cannot be changed (hatched areas in Fig. 23). The BEM model used for this case employs an initial mesh of 32 elements linear elements, and the internal points are placed only within the design area. All the cavities have prescribed Neumann homogeneous boundary condition. The process is halted when a volume ratio of 70 % between the final and the original designs is achieved. Figure 24 shows the topology history. It is worth to note that all previous examples could be solved by pure shape optimization, since the original topology is not changed. In the PCB case, however, new cavities are created during the process, characterizing truly topological changes in the domain. It is also interesting to note the creation of small cavities near the corners of the PCB. The present approach shows good agreement with the results obtained by Li et al. [15], as shown in Fig. 25.

4 Additional Comments

The outcomes stressed in the previous section show clearly that, although useful results can be obtained with the proposed methodology, it shares the same problems of most hard kill methods. If conveniently controlled, the designs obtained may be acceptable. However, it may be impossible to specify a sufficiently general material removal rule regardless the application. Furthermore, the imposition of constraints to the problem is rather complex, since the analytical expressions for D_T have been derived (in the original references) without considering them.

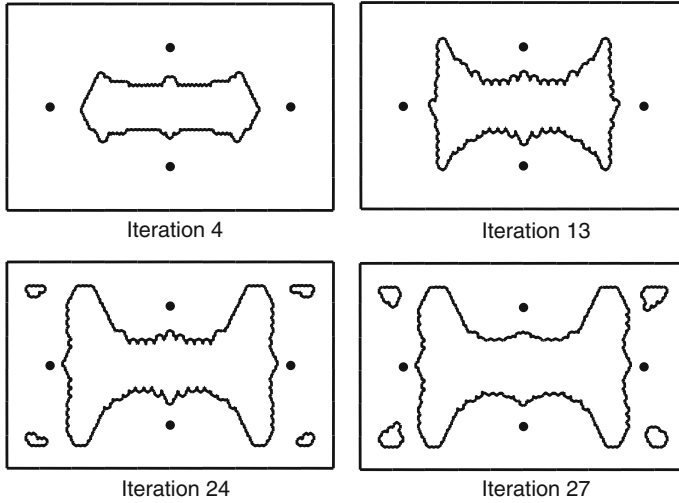


Fig. 24 Topology evolution for the PCB

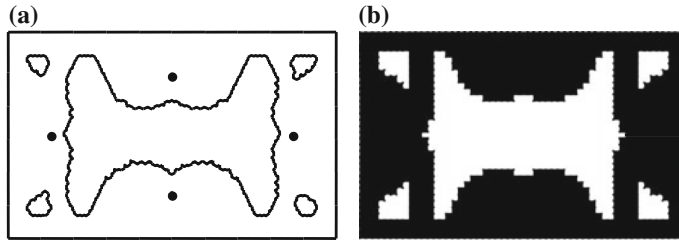


Fig. 25 Final topologies for the PCB: **a** Present results $-A_f = 0.70A_0$; **b** [15] $-A_f = 0.68A_0$

An important point in the present formulation is related to the relative magnitude of the D_T values as the iterative process evolves. After the first few iterations, the gradient of D_T along the domain becomes very low, since the optimal solution has constant sensitivities. Since some areas of the domain may be more affected by modeling and discretization errors than others, a fine tuning becomes mandatory to avoid material rejection at non-optimal locations. Another issue is related to the (non-mathematical) stopping criteria used. Specified volume fractions are relatively easy to implement. In the present approach, the current volume is compared with the target volume at the end of each iteration, and the process is halted if necessary (this is possible because the number of holes and the diameters are known during run time). Although useful for material saving, this criteria is devoid of further information like energy content or compliance values.

If, by one side, ESO methods show serious limitations, on the other side one can make interesting usages of D_T , particularly in conjunction with other optimization methods. For instance, if a surface of D_T values is constructed, its isolines can be used to specify a material rejection criteria. The domain obtained after that first iteration

can be a good starting point for SIMP methods or a shape optimization analysis. Generally the algorithm used to remove material leaves something to be desired, delivering unpleasantly jagged boundaries. “Tiling” schemes of material removal [5] has already proved to generate solutions very similar to the ones obtained with SIMP methods, and can be alternatively used. In any case, the smoothness of the resulting boundaries is more related to the size of the holes used to remove material. Regardless the type of hole (circular or squared), the resolution of boundaries generated will be finer when clouds of smaller holes are punched out of the design domain. However, this means a large number of internal points where D_T must be evaluated, increasing the computational cost of the analysis. The ideal situation relies on using holes large enough to accelerate the material removal but yet sufficiently small to capture all relevant geometric features of the optimal design. The sensitivity analysis is not directly affected by the size of the elements, provided the mesh is not too coarse (i.e. providing good results on internal points). The important aspect here is to keep the relative magnitudes of D_T reasonably well estimated along the whole design domain.

Another point to be highlighted here is the possibility of using post-processing algorithms to smooth the boundaries obtained not only with the BEM methodology shown here, but also to eliminate the see-saw aspect of most SIMP approaches reported. In this chapter a Bézier curve approach is employed avoiding boundaries irregularities. It is striking to note that the use of Bézier curves discards the need of a very fine mesh of internal grid points (very small holes).

5 Conclusions

Procedures for topology optimization are object of present research interest and several techniques have been proposed during last years. Despite the evolution of the present techniques of optimization, many drawbacks specific to each method still must be fixed. In this regard, this work employs topological sensitivity analysis and boundary elements for delivering optimized topologies as an alternative to the traditional optimization methods. Complex shapes with irregularities on their boundaries frequently result after a process of topology optimization. In this work, a Bézier smoothing technique is employed in order to avoid a new task of post-processing over the resulting topology due to the boundary irregularities. This procedure allows attaining more realistic geometries when the optimization is halted. The use of this technique provides optimized geometries suitable for direct manufacturing of the final design without major designer interference. A linear coordinate transformation method is also implemented, allowing the use of a D_T expression originally formulated only for isotropic materials also for non-isotropic materials. It is important to point out that the D_T has the potential total energy as an implicit cost function. The linear heat transfer for Laplace and Poisson problems are solved showing the feasibility of the procedure proposed and agreement with other solutions.

References

1. Mackerle, J.: Topology and shape optimization of structures using FEM and BEM: a bibliography (1999–2001). *Finite Elem. Anal. Des.* **39**, 243–253 (2003)
2. Bendsøe, M.P., Kikuchi, N.: Generating optimal topologies in structural design using a homogenization method. *Comput. Meth. Appl. Mech. Engrg.* **71**, 197–224 (1998)
3. Hassani, B., Hinton, E.: A review of homogenization and topology optimization III: topology optimization using optimality criteria. *Comput. Struct.* **69**, 739–756 (1998)
4. Novotny, A., Feijóo, R., Taroco, E., Padra, C.: Topological-shape sensitivity analysis. *Comput. Meth. Appl. Mech. Engrg.* **192**, 803–829 (2003)
5. Marczak, R.J.: Topology optimization and boundary elements: a preliminary implementation for linear heat transfer. *Eng. Anal. Bound. Elem.* **31**, 793–802 (2007)
6. Anflor, C.T.M., Marczak, R.J.: A boundary element approach for topology design in diffusive problems containing heat sources. *Int. J. Heat Mass Transf.* **52**, 4604–4611 (2009)
7. Anflor, C.T.M., Marczak, R.J.: Topological optimization of anisotropic heat conducting devices using Bézier-smoothed boundary representation. *Comput. Model. Eng. Sci.* **78**, 151–168 (2011) (Print).
8. Poon, K.C., Tsou, R.C.H., Chang, Y.P.: Solution of anisotropic problems of first class by coordinate-transformation. *J. Heat Transf.* **101**, 340–345 (1979)
9. Poon, K.C.: Transformation of heat conduction problems in layered composites from anisotropic to orthotropic. *Lett. Heat Mass Transf.* **6**, 503–511 (1979)
10. Newman, W.M., Sproull, R.F.: *Principles of Interactive Computer Graphics*. McGraw-Hill, New York (1982)
11. Brebbia, C.A., Dominguez, J.: *Boundary Elements: An Introductory Course*. Computational Mechanics Publications, Southampton (1988)
12. Banerjee, P.K.: *The Boundary Element Methods in Engineering*. McGraw-Hill College, New York (1994)
13. Harrington, S.: *Computer Graphics: A Programming Approach*. McGraw-Hill, New York (1983)
14. Park, Y.K.: Extensions of optimal layout design using the homogenization method. Ph.D. Thesis, The University of Michigan, East Lansing Michigan (1995).
15. Li, Q., Steven, G., Querin, O., Xie, Y.: Shape and topology design for heat conduction by evolutionary structural optimization. *Int. J. Heat Mass Transf.* **42**, 3361–3371 (1999)

Optimization of Structures and Components

Muñoz-Rojas, P.A. (Ed.)

2013, VII, 141 p. 80 illus., 32 illus. in color., Hardcover

ISBN: 978-3-319-00716-8